PCCP

PAPER

View Article Online
View Journal | View Issue

Cite this: *Phys. Chem. Chem. Phys.*, 2016, **18**, 13074

Microwave-enhanced electrochemical cycling performance of the $LiNi_{0.2}Mn_{1.8}O_4$ spinel cathode material at elevated temperature

Kumar Raju,[a] Funeka P. Nkosi,[ab] Elumalai Viswanathan,[c] Mkhulu K. Mathe,[a] Krishnan Damodaran[c] and Kenneth I. Ozoemena*[ab]

The well-established poor electrochemical cycling performance of the $LiMn_2O_4$ (LMO) spinel cathode material for lithium-ion batteries at elevated temperature stems from the instability of the Mn^{3+} concentration. In this work, a microwave-assisted solid-state reaction has been used to dope LMO with a very low amount of nickel (*i.e.*, $LiNi_{0.2}Mn_{1.8}O_4$, herein abbreviated as LMNO) for lithium-ion batteries from Mn_3O_4 which is prepared from electrolytic manganese oxide (EMD, γ-MnO_2). To establish the impact of microwave irradiation on the electrochemical cycling performance at an elevated temperature (60 °C), the Mn^{3+} concentration in the pristine and microwave-treated LMNO samples was independently confirmed by XRD, XPS, ^{6}LiMAS-NMR and electrochemical studies including electrochemical impedance spectroscopy (EIS). The microwave-treated sample ($LMNO_{mic}$) allowed for the clear exposure of the {111} facets of the spinel, optimized the Mn^{3+} content, promoting structural and cycle stability at elevated temperature. At room temperature, both the pristine (LMNO) and microwave-treated ($LMNO_{mic}$) samples gave comparable cycling performance (>96% capacity retention and *ca.* 100% coulombic efficiency after 100 consecutive cycling). However, at an elevated temperature (60 °C), the $LMNO_{mic}$ gave an improved cycling stability (>80% capacity retention and *ca.* 90% coulombic efficiency after 100 consecutive cycling) compared to the LMNO. For the first time, the impact of microwave irradiation on tuning the average manganese redox state of the spinel material to enhance the cycling performance of the $LiNi_{0.2}Mn_{1.8}O_4$ at elevated temperature and lithium-ion diffusion kinetics has been clearly demonstrated.

Received 20th March 2016,
Accepted 11th April 2016

DOI: 10.1039/c6cp01873d

www.rsc.org/pccp

Introduction

Rechargeable lithium-ion batteries (RLIBs) have emerged as the most dominant power sources for portable electronics and electric vehicles and will remain so for many years to come. Spinel, layered and olivine materials are the most important cathode materials for the RLIBs. Manganese-based spinel materials have become more attractive due to their inherent advantageous properties such as earth-abundance, low-cost, environmental benignity and satisfactory thermal stability.[1–6] Lithium manganese oxide, $LiMn_2O_4$ (LMO), a spinel cathode material for RLIBs is a cathode material that drives some electric vehicles (*e.g.*, Nissan Leaf and Chevrolet Volt). Two main challenges that this cathode material still confront are (i) the disproportionation reaction and (ii) Jahn–Teller effects, especially at elevated temperatures (55 °C). Indeed, the LMO combined with a robust spinel framework exhibits an astonishing cycle life associated with substantial capacity retention at room temperature, which has been intensively studied.[7–11] However, the LMO suffers from rapid capacity-fading with cycling due to the manganese-dissolution at an elevated temperature which limits the practical use of this spinel material for large-scale applications. In particular, the manganese-dissolution is owed to the disproportionate reaction of Mn^{3+} with Mn^{2+} and Mn^{4+} ions; Mn^{2+} dissolves into the electrolyte, gets reduced to a metal and deposited as a film on the surface of the anode, whilst Mn^{4+} promotes the electro–inactive layer on the cathode side, creating defects in the lattice.[12–17]

Disproportional reaction:

$$2Mn_{(solid)}^{3+} \rightarrow Mn_{(solid)}^{4+} + Mn_{(solution)}^{2+} \quad (1)$$

These properties of the Mn ions lead to capacity-fading during cycling at elevated temperatures. Thus, despite the fact that Mn^{3+} can improve the conductivity of the spinel cathode material, it is now well-recognised that the amount of Mn^{3+}

[a] *Energy Materials, Materials Science and Manufacturing, Council for Scientific and Industrial Research (CSIR), Pretoria 0001, South Africa. E-mail: kozoemena@csir.co.za*
[b] *Molecular Sciences Institute, School of Chemistry, University of the Witwatersrand, Johannesburg PO Wits 2050, South Africa*
[c] *Department of Chemistry, University of Pittsburgh, Pittsburgh, PA 15260, USA*

in the spinel structure must be kept at an appropriate level to curb capacity-fading at elevated temperature. There have been several strategies proposed in the literature to minimize capacity-fading in LMO, which include the following; (i) surface-coating of LMO with metal oxides,[18,19] (ii) coating LMO with specific metals (Bi, Pb, La, Ba, Zr, Y, Sr, Zn and Mg),[20] (iii) simultaneous doping with aluminium and fluorine,[21] (iv) the surface-treatment process of nickel-doped LMO (LMNO) powder utilizing two strong acids, hydrofluoric acid (HF) and phosphoric acid (H_3PO_4),[22] (v) coating lithium-rich LMO with LMNO,[23] (vi) co-doping of LMO with aluminium and nickel *via* the so-called thermopolymerisation method with acrylic acid,[24] and (vii) the addition of mixed additives (bis(dialkylamino)naphthalene and vinylene carbonate) to the electrolyte.[25] On the other hand, the research groups of Manthiram[26] and Chen[27] have also demonstrated that LMNO with predominant surface {111} facets exhibited improved cycling performance as exposed {111} facets allow the formation of a thinner solid electrolyte interphase (SEI) than other facets.

The above named strategies for ameliorating capacity-fading in LMO at elevated temperature are either time-consuming or involve the extensive use of materials that could add to the cost of the final cathode material, and/or require the use of less environmentally-friendly chemicals including very harsh acids that must be handled with utmost caution. In this work, we have chosen 0.2 nickel (*i.e.*, Mn : Ni = 9) since it has been shown that such a mole ratio is capable of stabilizing the M–O bonding in the [MnO_6] octahedron than other mole ratios, leading to enhanced performance in electrochemical cycling.[28] Therefore there is a need to explore the use of a simpler, fast, less expensive and 'greener' synthesis strategy. Motivated by this need, coupled with the realisation that the LMO chemistry can be improved by nickel-doping[28,29] and microwave-irradiation,[30,31] this new study demonstrates that by doping LMO with a very small amount of nickel ($LiMn_{1.8}Ni_{0.2}O_4$) and subjecting it to microwave irradiation, one is able to manipulate the Mn^{3+}/Mn^{4+} concentrations, expose the prominent {111} facets, stabilize the spinel structure, and enhance the cycling performance at an elevated temperature (60 °C). To our knowledge, this is the first report of the use of microwave-assisted preparation of doped-LMO for improving the performance of LMO under high temperature operating conditions. Interestingly, $LiMn_{1.8}Ni_{0.2}O_4$ was obtained from an industrially-preferred solid-state method using Mn_3O_4 obtained from low-cost electrolytic manganese oxide (EMD, γ-MnO_2).

Experimental

Reagents and synthesis of LMNO and $LMNO_{mic}$

First, the manganese precursor material (Mn_3O_4) was obtained from electrolytic manganese dioxide (MnO_2 = 92.46% purity, Delta EMD (Pty) Ltd, South Africa) by using the established method of high-temperature annealing at 1050 °C in air for 74 h.[32] The purity and morphology of Mn_3O_4 were established from SEM, TEM and XRD. NiO (>99% pure), Li_2CO_3 (>99% pure) and urea (>99% pure) were obtained from Sigma-Aldrich and used without further treatment. $LiNi_{0.2}Mn_{1.8}O_4$ (LMNO) was synthesized using a similar method reported by Yang *et al.*[33] In brief, stoichiometric amounts of reagents Li_2CO_3, NiO and the as-prepared Mn_3O_4 (molar ratio of Li : Mn : Ni = 1.15 : 1.8 : 0.2) were ground using a mortar and pestle. A 10% excess of Li_2CO_3 was used to compensate for the easy loss of Li at high temperature heating. Urea (0.57 M per lithium) was added to the mixture and then ground to fine powder. The mixture was then preheated at 500 °C for about 7 min. Upon cooling down to room temperature in air, the preheated spinel precursor was ground into fine powder and then divided into two equal portions; the first portion was directly annealed at 900 °C for 6 h, while the second portion was subjected to microwave irradiation at 600 W for 20 min (using the Anton Paar Multiwave 3000 system, λ = 0.12236 m) before annealing at 900 °C for 6 h. The spinel materials without and with microwave irradiation are abbreviated herein as LMNO and $LMNO_{mic}$, respectively.

Characterization techniques

The XRD patterns of the as-prepared Mn_3O_4, LMNO and $LMNO_{mic}$ were obtained from a PANalytical X'Pert PRO diffractometer equipped with Ni-filtered Cu K-alpha radiation (λ = 1.541841 Å). X-ray photoelectron spectroscopy (XPS) was performed for LMNO and $LMNO_{mic}$ using a non-monochromatic aluminum (Al) Kα source (1486.6 eV) and an Al monochromatic Kα source (1486.6 eV), respectively. The XPS data analysis was performed with the XPS Peak 4.1 program and a Shirley function was used to subtract the background. The morphology of the as-synthesized powders was analysed using a JEOL-JSM 7500F scanning electron microscope operated at 2.0 kV. TEM and HRTEM images were obtained from a JEOL-Jem 2100 microscope operated at an acceleration voltage of 200 kV. All the NMR experiments were performed on a Bruker Avance 500 MHz (B_0 = 11.7 Tesla) Wide bore spectrometer. ^{6}Li and ^{7}Li NMR measurements were done at corresponding Larmor frequencies of 73.59 and 194.36 MHz respectively using a 3.2 mm CPMAS probe. ^{6}Li NMR was collected using a rotor synchronized Hahn echo sequence (90-tau-180-tau acquisition) at a 20 kHz spinning speed. 90° pulse lengths of 6 μs and a relaxation delay of 0.5 s were used. ^{7}Li NMR was collected using a single pulse at MAS rates of 17, 20, 23 kHz for identifying the center bands. 2 μs pulse was used for excitation (90° pulse was 4.6 μs) and a relaxation delay of 0.5 s was used. All the spectra were referenced to standard 1 M LiCl solution at 0 ppm. All the electrochemical analyses were carried out in a coin cell (LIR-2032) fabricated with as-prepared LMNO and $LMNO_{mic}$ as the positive electrodes and lithium metal foil as the negative using a MACCOR series 4000 tester. The positive electrodes were prepared by coating the slurry mixture of the electrode material, acetylene black and polyvinylidene fluoride (80 : 10 : 10) onto a cleaned and polished aluminium foil, and dried in a vacuum oven at 80 °C overnight. The cells were assembled in an argon-filled MBraun® glovebox (O_2, H_2O < 0.5 ppm). The electrolyte was 1 M $LiPF_6$ in a mixture of 1 : 1 (v/v) ethylene carbonate (EC)/dimethyl carbonate (DMC) while Cellgard 2300 was used as the separator. The cyclic

voltammetry (CV) and electrochemical impedance (EIS) analysis were carried out on a Bio-Logic VMP3 potentiostat/galvanostat controlled by EC-Lab v10.40 software.

Results and discussion

Fig. 1a shows the XRD pattern of the as-prepared Mn_3O_4 with peaks that can be indexed to the tetragonal Mn_3O_4 spinel (JCPDS no: 80-0382) with space group $I4_1/amd$. The obtained well-defined reflections with no impurity phases indicate that the as-prepared Mn_3O_4 is highly crystalline. Fig. 1b shows the XRD profiles of LMNO and $LMNO_{mic}$ with their Rietveld refinement. This confirms that the prepared materials have typical single phase spinel structures, which adopt the $Fd\bar{3}m$ space group with lithium and transition metals located in 8a and 16d sites respectively. The calculated lattice parameters of the pristine (a = 8.211 Å) and microwave treated (a = 8.213 Å) are essentially the same and are in agreement with the literature.[34] All the three axes of cubic spinel are the same, thus $a = b = c$. We performed Rietveld refinement with R_p = 2.278 and R_{wp} = 2.922 for the LMNO, and R_p = 2.338, R_{wp} = 2.987 values for the $LMNO_{mic}$ powders. A closer look at the XRD profiles (Fig. 1c–e) indicates that the $LMNO_{mic}$ shows less intense peaks than the pristine LMNO, which suggests that the value of full width at half maximum (FWHM) for the LMNO-mic will be somewhat larger for the $LMNO_{mic}$ and it contains smaller sized particles compared to the LMNO.

Fig. 2 depicts the morphological evolutions (SEM and TEM images) of the Mn_3O_4, LMNO and LMNO-mic samples. It is clear from the figures that the as-prepared Mn_3O_4 exhibits a tetragonally-distorted spinel morphology in micron size (Fig. 2a). From the HRTEM image of lattice fringes (Fig. 2b), it has an average neighbouring fringe with a distance of 0.234 nm, corresponding to the {011} facets. This is also confirmed by using SAED patterns (Fig. 2c).

Fig. 2d–g show the SEM images of LMNO, the magnified view of one well-defined octahedron particle display {111} facets (Fig. 2g) and the HRTEM image of the lattice fringe of LMNO of 0.332 nm. Fig. 2h–m show the SEM images of $LMNO_{mic}$, the magnified view of one well-defined octahedron particle display {111} facets (Fig. 2m) and the HRTEM image of the lattice fringe of LMNO of 0.316 nm with corresponding SAED patterns of $LMNO_{mic}$ (Fig. 2l). Although the SEM images of LMNO and LMNO-mic exhibited almost the same octahedron morphology, there is a slight change in the particle sizes. Generally, the $LMNO_{mic}$ shows smaller sized particles (<1 μm) while those of the LMNO are in the 1 μm range. From HRTEM studies, it was difficult to observe smaller sized particles for the LMNO whereas the $LMNO_{mic}$ (Fig. 2j and k) easily showed

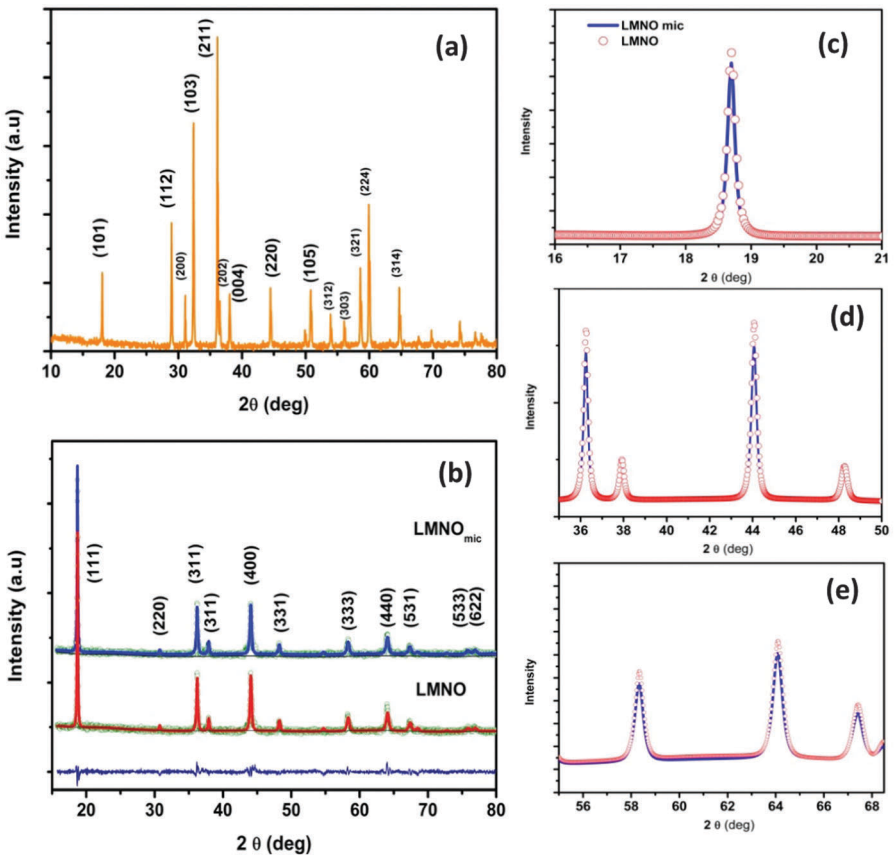

Fig. 1 Structural characterization of Mn_3O_4, LMNO and $LMNO_{mic}$: (a) the XRD profile of Mn_3O_4, (b) XRD patterns of LMNO and $LMNO_{mic}$ with Rietveld refinement, while (c–e) are the magnified view of LMNO and $LMNO_{mic}$ powders showing the intensity variation between them.

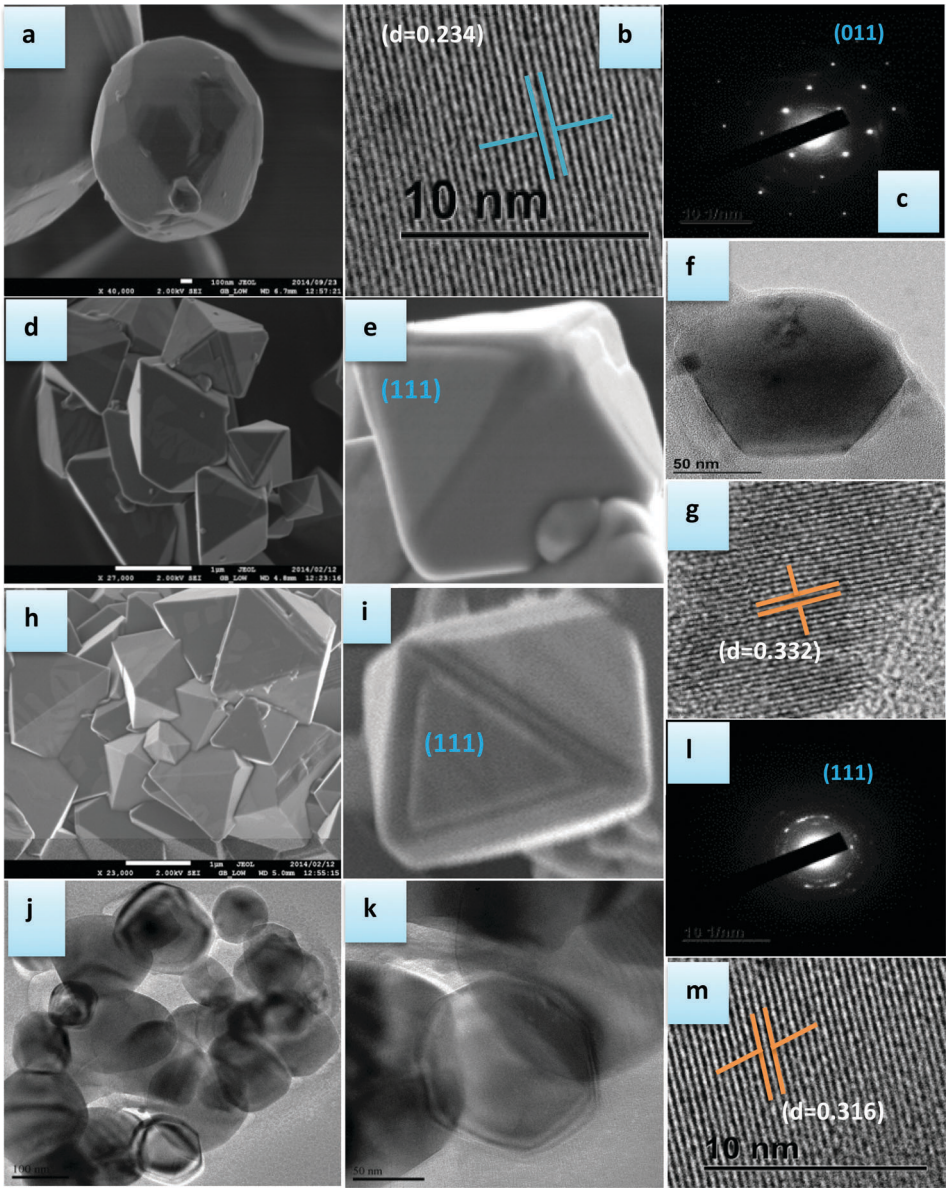

Fig. 2 Morphological evolution of Mn_3O_4, LMNO and LMNO-mic: (a–c) SEM and HRTEM images of Mn_3O_4 with corresponding SAED patterns, (d–g) SEM and TEM and HRTEM images of LMNO with a single nano-octahedron of LMNO (e). (h–m) SEM and TEM and HRTEM images of $LMNO_{mic}$ with a single nano-octahedron of $LMNO_{mic}$ (i), and with corresponding SAED patterns of $LMNO_{mic}$ (m).

particles with small sizes (100–200 nm range). EDX confirmed the stoichiometry of LMNO and $LMNO_{mic}$ as $LiMn_{1.8}Ni_{0.2}O_4$.

Fig. 3 compares the XPS of deconvoluted Mn $2p_{3/2}$ peaks of the LMNO and $LMNO_{mic}$ samples. Each of the deconvoluted spectra gives two binding energy values corresponding to the characteristic peaks of Mn^{3+}/Mn^{4+} at 642.17/643.59 and 642.43/644.12 eV, and the values are very close in accordance with reported values. The Ni 2p peak could not be viewed owing to its low intensity as a result from the low Ni content in the samples. Table 1 summarizes the XPS data, including the ratio of Mn^{3+}/Mn^{4+} and manganese valence of the LMNO and $LMNO_{mic}$. From the XPS data in Table 1, the $LMNO_{mic}$ contains more of Mn^{4+} in its structure than in the LMNO. Evidently, microwave irradiation was able to tune the ratio of Mn^{3+}/Mn^{4+} from 2.41 (for LMNO) to 1.75 (for $LMNO_{mic}$), with the manganese average redox state (Mn valence) being 3.29 and 3.36 for LMNO and $LMNO_{mic}$, respectively.

Solid-state ^6Li Magic Angle Spinning Nuclear Magnetic Resonance (^6Li MAS-NMR) spectroscopy is highly sensitive to the local environment of the Li ion. ^6Li MAS-NMR analyses were performed on LMNO and $LMNO_{mic}$ in order to investigate the effect of microwave irradiation on the local environment of Li ions. Fig. 4 illustrates the ^6Li MAS-NMR spectra of LMNO and $LMNO_{mic}$ that were recorded at a spinning speed of 20 kHz. The dominant interactions between Li nuclear spins and Mn electron spins are either through-bond (Fermi-contact) or through-space (dipolar) interactions. Fermi-contact interactions shift Li NMR resonances to >500 ppm, whereas the electron-nuclear dipolar

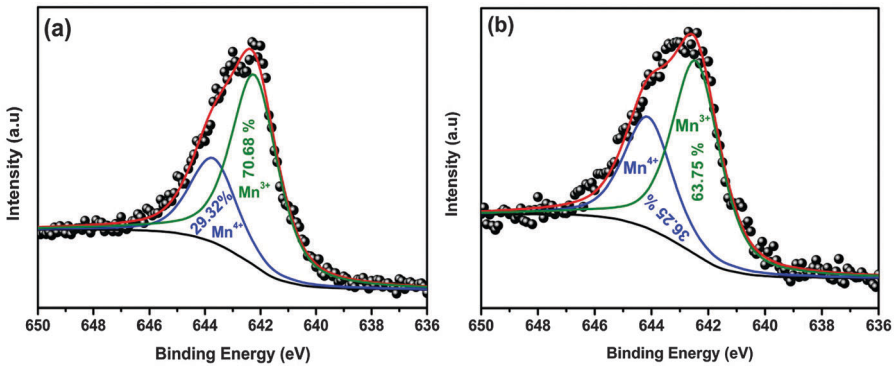

Fig. 3 XPS spectra obtained for (a) LMNO and (b) $LMNO_{mic}$.

Table 1 XPS (Mn-$2p_{3/2}$ spectra) data of the LMNO and $LMNO_{mic}$ samples

Sample	Binding energy position (eV)		Cation distribution			Mn valence (average redox state)
	Mn^{4+}	Mn^{3+}	Mn^{4+} (%)	Mn^{3+} (%)	Mn^{3+}/Mn^{4+}	
LMNO	643.59	642.17	29.32	70.68	2.41	3.293
$LMNO_{mic}$	644.12	642.43	36.25	63.75	1.75	3.363

interactions give rise to large spinning sideband patterns during MAS-NMR. For instance, the spinel $LiMn_2O_4$ gives major resonance of Li nuclei around ~520 ppm corresponding to the mixed-valence of Mn^{3+} and Mn^{4+} ions (the average oxidation state of $Mn^{3.5+}$, *i.e.*, cation distribution is 50% Mn^{3+} and 50% Mn^{4+}). If the average oxidation state of Mn (*i.e.*, Mn valence) around the local lithium site is increased, then the lithium chemical shift moves further downfield of 520 ppm.[35–37] This increase in the oxidation state of manganese ions in the local environment of lithium results in a shift of the resonance to higher frequency. As shown in Fig. 4, two major ^6Li resonances are observed at 528.4 and 482.0 ppm for $LMNO_{mic}$ and 528.0 and 478.2 ppm for LMNO, which can be assigned to the tetrahedrally coordinated Li^+ surrounded by Ni^{2+} and Mn^{4+} ions.[38] The slight shift of the peaks to the lower frequencies is attributed to the increased Mn^{3+} content in the LMNO. Importantly, the peaks in the high frequency region (750–850 ppm) are due to Mn^{4+}, thus the broad high frequency resonance observed at 814.3 ppm for the $LMNO_{mic}$ clearly indicates that the microwave irradiation causes a further increase in Mn^{4+} concentration around Li^+ which, in turn, results in the chemical shift of lithium resonance moving further downfield. Indeed, the ^6Li MAS-NMR spectra clearly corroborate

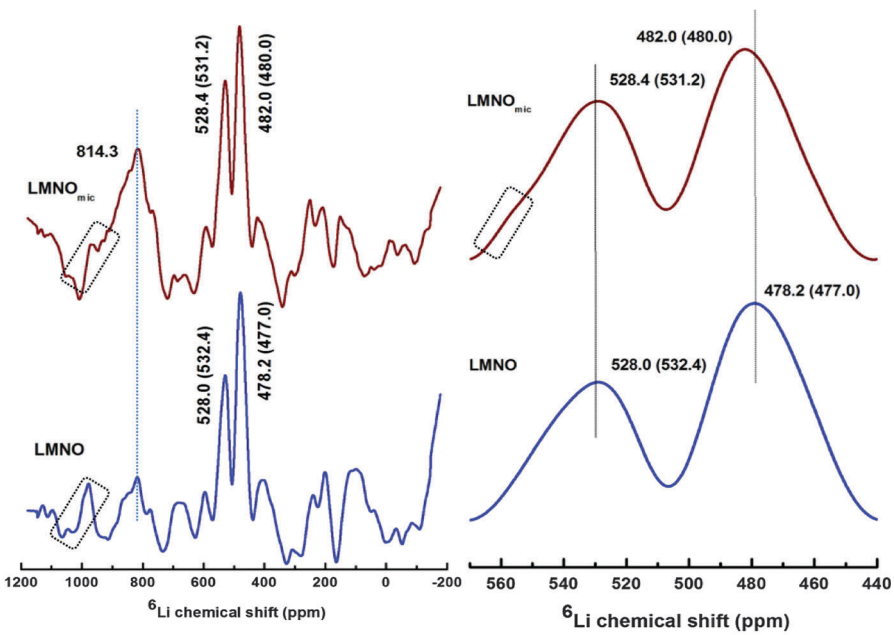

Fig. 4 ^6Li MAS NMR spectra of LMNO and $LMNO_{mic}$ with the expended view of 560–440 ppm.

the XPS and XRD results that predict higher concentration of the Mn^{3+} in the LMNO than in the $LMNO_{mic}$ spinel structure.

Cyclic voltammetry (CV) studies were performed on LMNO and $LMNO_{mic}$ at room temperature at a scan rate of 0.1 mV s^{-1} in order to investigate the diffusion kinetics of lithium. Fig. 5a illustrates the CV profiles of LMNO and $LMNO_{mic}$ recorded in the potential window of 2 to 4.9 V *vs.* Li/Li^+ that display very prominent anodic and cathodic peaks corresponding to the lithium extraction and insertion kinetics. The well-resolved pair of anodic peaks at 4.73 and 4.8 and their corresponding cathodic peaks at 4.6 and 4.7 V are related to the oxidation of Ni^{2+}/Ni^{3+} and Ni^{3+}/Ni^{4+} as well as Li extraction/insertion processes. Similarly, the shoulder peaks observed for both anodic (4.12 and 4.24 V) and cathodic (3.89 and 4.05 V) regions are characteristic of Mn^{3+}/Mn^{4+} redox reactions despite having a small difference in cathodic peaks (3.87 and 4.06 V) for the microwave irradiated sample. It is noteworthy to mention that the anodic peak obtained at 3.85 V associated with the extraction of lithium resides at the octahedral sites. The peak intensity increases with an increase in cycling as a result of an incomplete extraction of lithium that occupies the octahedral sites at 3.12 V. In addition, the strong peaks resolved at 3.1 V for the anodic region and at 2.73 V for the cathodic region imply that the intercalation of lithium is more pronounced even below 3 V, the sharp peaks indicate that the as-prepared spinel has substantial stability even below 3 V.

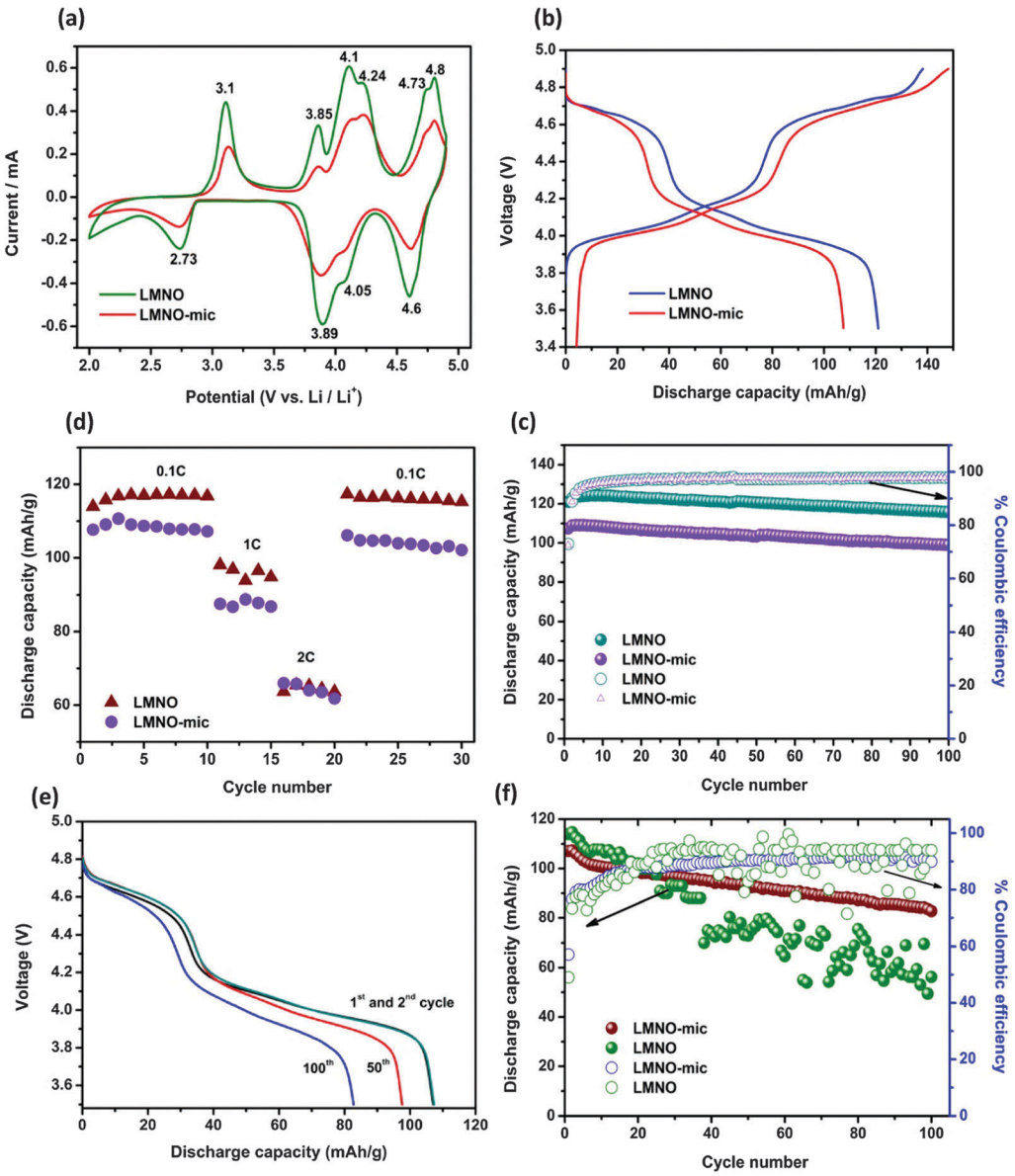

Fig. 5 Electrochemical analysis of LMNO and $LMNO_{mic}$ at room temperature and at 60 °C. (a) Cyclic voltammetry at a scan rate of 1 mV s^{-1} (b) charge–discharge at a current density of 0.1C (c) prolonged cycling with coulombic efficiency at room temperature at a current density of 0.1C (d) rate capability at different current densities (e) discharge curves of $LMNO_{mic}$ with a current density of 0.1C at 60 °C and (f) prolonged cycling of $LMNO_{mic}$ with coulombic efficiency at a current density of 0.1C at 60 °C.

Fig. 5b compares the galvanostatic charge–discharge of LMNO and $LMNO_{mic}$ samples at room temperature. The curves are typical signatures of $LiMn_{1.8}Ni_{0.2}O_4$.[29] The well-defined plateaus around 4.73, 4.12 and 4.05 V regions for both samples confirm the redox reactions of Ni and Mn. The pristine and microwave irradiated samples delivered comparable specific capacities of 121 and 108 mA h g^{-1} at room temperature, respectively. Both samples retained more than 95% of their initial capacity after 100 cycles and maintained excellent coulombic efficiency (Fig. 4c). Fig. 5d showed that both samples showed comparable rate capability, especially at 2C. At an elevated temperature of 60 °C (Fig. 5e & f), the $LMNO_{mic}$ outperformed the pristine LMNO-based cell, with a specific capacity of 108 mA h g^{-1} and good cycling stability, retaining ~80% of its initial capacity with 90% coulombic efficiency after 100 repeated cycles. The LMNO delivered an initial capacity of 118 mA h g^{-1} at 60 °C but the cycling stability is very poor, retaining about 40% of its initial capacity after 100 cycles. At room temperature, both LMNO and $LMNO_{mic}$ exhibited almost similar electrochemical performances in terms of specific capacity and capacity retention. The microwave-treated spinel with a slightly higher average Mn redox state exhibited good cycle stability at 60 °C than the pristine LMNO. We may conclude that the high capacity retention of the $LMNO_{mic}$ at elevated temperature is due to the ability of the microwave irradiation to tune the Mn valence or the Mn^{3+}/Mn^{4+} ratio to an appropriate level for enhanced electrochemical performance. The poor performance of the LMNO at 60 °C may be related to its higher Mn^{3+} content which may be taking part in the disproportionation reaction. Despite the fact that both spinel materials have the same surface {111} facets, the slightly higher content of Mn^{3+} in pristine may still allow the disproportionation reaction to occur.

To provide further insights into the effects of microwave-treatment on the spinel materials, EIS experiments were carried out on LMNO- and $LMNO_{mic}$-based coin cells at different voltages after the freshly prepared cells were relaxed at OCV for 1 h. Fig. 6a–d illustrate the Nyquist plots of LMNO and $LMNO_{mic}$ obtained before and after 50 charge–discharge cycles at 60 °C. All the obtained EIS curves were satisfactorily fitted with an electrical equivalent circuit shown in Fig. 6e. The fitting parameters consist of a depressed semicircle at a high and intermediate frequency domain related to the solid–electrolyte interface (SEI) whose resistance is denoted as R_f, constant-phase element of surface film (Q_f or CPE_f), interfacial capacitance (C_{Li}), the solution bulk resistance (R_s), the charge transfer resistance of Li ion insertion and extraction (R_{Li}), the Warburg impedance (Z_w) due to the Li ion diffusion in the solid state.[39–42] As seen in Fig. 6a–d, the formation of a SEI layer becomes more stable for $LMNO_{mic}$ at all the voltage range at the elevated temperature after 50 consecutive charge–discharge cycles, which results in the appearance of a high frequency semicircle at all potentials investigated. The thin SEI layer formed may be because the octahedral shaped particles with {111} facets suppress the co-insertion of the electrolyte and deliver larger lithium diffusion.[43] Tables 2 and 3 summarise the values from the fitted Nyquist plots using the EEC for the LMNO and $LMNO_{mic}$, respectively. From Fig. 6 and Tables 2 and 3, it is evident that the poor cycling performance of the LMNO at elevated temperature may be related to a systematic rise in impedance arising from Mn^{3+} dissolution.

Lithium diffusion coefficients (D_{Li}) of the LMNO- and $LMNO_{mic}$-based coin cells were determined before and after 50 consecutive cycles at 25 °C and 60 °C respectively by using equation (eqn (2) and (3)) with Warburg impedance, σ, obtained from the slope of real impedance (Z') *vs.* reciprocal square root of frequency ($\omega^{-1/2}$) in the low frequency region.[44]

$$D_{Li} = \frac{2R^2T^2}{n^4F^4\sigma^2A^2C_{Li}^2} \quad (2)$$

$$Z_\omega = \sigma(1 - j)\omega^{-1/2} \quad (3)$$

where R is the gas constant, T is the absolute temperature, n is the number of electrons transferred per molecule during oxidation, F is the Faraday constant, C_{Li} is the lithium concentration in the cathode material and A is the geometric surface area of the cathode. The diffusion coefficients calculated at 4.2 V are found to be 3.32×10^{-13}, 1.6×10^{-12}, 2.8×10^{-12} and 5.1×10^{-12} cm^2 s^{-1} at room temperature for LMNO, $LMNO_{mic}$ and their respective values after 50 charge–discharge cycles and the obtained values are in accordance with the values reported in the literature.[42] At 60 °C, the spinel revealed the D_{Li} of 2.03×10^{-12} and 7.93×10^{-12} cm^2 s^{-1} for LMNO and $LMNO_{mic}$ respectively, and 1.38×10^{-13} and 3.19×10^{-12} cm^2 s^{-1} for LMNO and $LMNO_{mic}$ after 50 repeated cycles, respectively. The microwave treated spinel materials have high diffusion coefficients even after prolonged cycling than the pristine.

It is perhaps necessary to emphasize that while Mn^{3+} improves electronic conductivity; its content must be controlled to curb the negative effects of the disproportionation reaction (eqn (1)) and the accompanying severe capacity-fading at elevated temperatures. Indeed, there is a lot of evidence in the literature which prove that the higher content of surface Mn^{3+} leads to disproportionation of Mn^{3+} and severe capacity-fading despite the increased electronic conductivity.[45] Our finding agrees with the need to have an ''appropriate'' amount of Mn^{3+} to get the best performance. For example, Zheng *et al.*[46] clearly stated as follows: ''the presence of an appropriate amount of oxygen deficiency and/or Mn^{3+} is critical to accelerate the Li^+ ion transport within the crystalline structure''. In addition, it is to be noted that the enhancement of Li^+ ion transport is not just a factor of the Mn^{3+} content, but other factors such as the morphology and particle size.[31,47] Smaller sized particles are known to offer a short path length for Li^+ to travel within the crystalline structure, and $LMNO_{mic}$ gave smaller sized particles than pristine LMNO. The well-defined octahedron morphology with {111} facets in the $LMNO_{mic}$ crystal structure, coupled with the local environment of the Li-ion in the spinel structure (evident from the ^6Li MAS-NMR spectra, whereby Li^+ is surrounded by Mn^{4+} and the highly conductive Ni^{2+}) could have also enhanced the Li^+ diffusivity.

Microwave chemistry occurs by two main mechanisms; dipolar polarization (alignment of dipoles in the microwave field) and

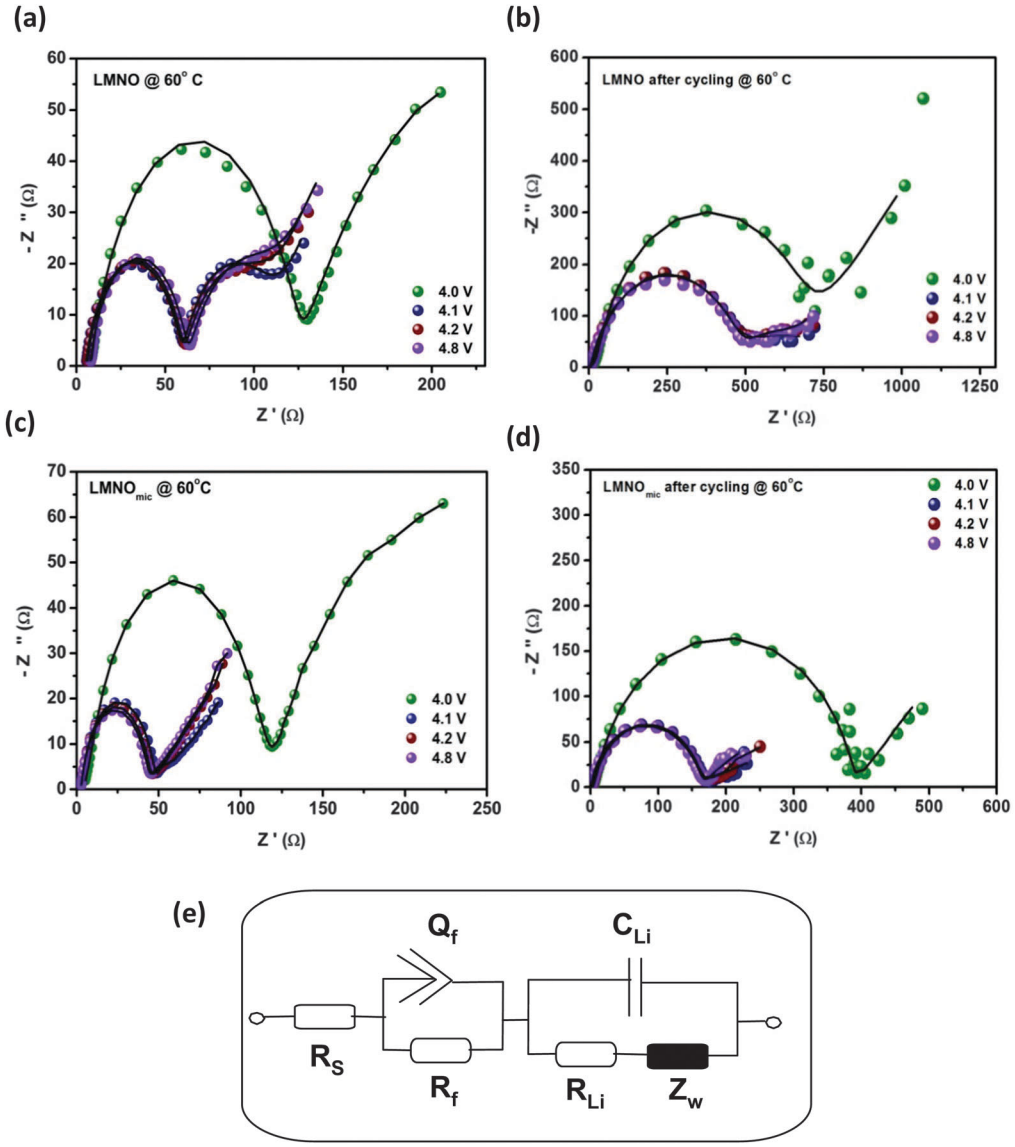

Fig. 6 Electrochemical impedance spectra of LMNO and LMNO$_{mic}$ at different voltage ranges (a and c) before (b and d) after 50 cycles at 60 °C. The electrical equivalent circuit used in fitting the Nyquist plots is shown as (e).

Table 2 Summary of EIS parameters for the LMNO based coin cells; all values were obtained from the fitted impedance spectra after several iterations using the proposed equivalent electrical circuit shown in Fig. 6

	EIS data for LMNO @ 60 °C						
Applied potential (V)	R_s (Ω)	R_f (Ω)	CPE (μF)	n	C_{Li} (mF)	R_{Li} (Ω)	Z_w (Ω $\omega^{-1/2}$)
Before cycling							
4.0	8.25 ± 0.43	49.51 ± 6.48	25.93 ± 2.02	0.72 ± 0.14	13.7 ± 1.8	120 ± 1.26	20.36 ± 0.8
4.1	7.78 ± 0.52	41.84 ± 6.86	17.44 ± 0.75	0.73 ± 0.05	14.53 ± 5.76	54.64 ± 1.8	8.10 ± 0.97
4.2	6.05 ± 0.45	54.53 ± 2.06	15.79 ± 6.59	0.72 ± 0.18	11.6 ± 0.76	49.77 ± 3.64	6.94 ± 0.86
4.8	5.54 ± 0.45	54.08 ± 2	17.08 ± 7.09	0.78 ± 0.21	9.51 ± 0.43	51.67 ± 2.49	5.22 ± 0.78
After 50th cycle							
4.0	11.14 ± 0.57	762 ± 3	8.13 ± 0.42	0.72 ± 0.24	17.24 ± 1.42	236 ± 6	34.21 ± 1.24
4.1	6.35 ± 0.84	531 ± 7	6.42 ± 0.74	0.67 ± 0.17	11.9 ± 1.34	241 ± 3	28.87 ± 3.72
4.2	2.62 ± 0.65	515 ± 15	1.35 ± 0.28	0.68 ± 0.51	10.08 ± 1.04	383 ± 17	47.55 ± 0.78
4.8	5.43 ± 0.53	549 ± 20	5.92 ± 0.48	0.75 ± 0.57	1.41 ± 0.26	260 ± 4	36.98 ± 2.53

ionic conduction (movement of ions in the microwave field) that ultimately led to the generation of heat energy.[48] From our findings, microwave irradiation seems to have a significant impact on the redox chemistry of the spinel whereby the 'excess'

Table 3 Summary of EIS parameters of the $LMNO_{mic}$-based coin cells; all values were obtained from the fitted impedance spectra after several iterations using the proposed equivalent electrical circuit shown in Fig. 6

	EIS data for LMNO-mic @ 60 °C						
Applied potential (V)	R_s (Ω)	R_f (Ω)	CPE (μF)	n	C_{Li} (mF)	R_{Li} (Ω)	Z_w (Ω $\omega^{-1/2}$)
Before cycling							
4.0	2.76 ± 0.34	11.15 ± 2.63	9.58 ± 0.45	0.72 ± 0.03	9.69 ± 0.9	46.51 ± 2.53	6.27 ± 2.62
4.1	2.58 ± 0.41	20.58 ± 3.57	9.37 ± 6.4	0.67 ± 0.13	25.5 ± 5.4	46.46 ± 3.91	10.07 ± 0.7
4.2	2.59 ± 0.39	17.13 ± 1.7	33.56 ± 18.05	0.52 ± 0.07	9.16 ± 6.6	42.46 ± 3.77	7.2 ± 2.4
4.8	5.15 ± 0.42	132.3 ± 20.6	12.41 ± 0.47	0.72 ± 0.15	11.44 ± 1.94	114 ± 1.68	12.97 ± 1.44
After 50th cycle							
4.0	4.13 ± 0.48	409.3 ± 2.23	9.74 ± 0.68	0.63 ± 0.05	5.44 ± 0.26	272.3 ± 9.42	51.66 ± 13.19
4.1	3.86 ± 0.21	173.35 ± 2.54	10.23 ± 0.57	0.61 ± 0.18	3.63 ± 0.38	94.68 ± 2.81	32.24 ± 5.34
4.2	2.17 ± 0.34	164.71 ± 1.72	8.71 ± 1.73	0.64 ± 0.13	7.11 ± 1.53	105.41 ± 5.26	29.89 ± 2.71
4.8	1.86 ± 0.51	179.43 ± 2.78	9.18 ± 0.82	0.69 ± 0.57	4.69 ± 0.86	96.82 ± 2.37	36.22 ± 4.39

Mn^{3+} is converted to Mn^{4+} for enhanced electrochemistry (notably, cycling durability and Li^+ diffusion) at elevated temperature. However, further studies are necessary to fully explore this mechanism, and these will constitute the next steps of our future research activities on the topic.

Conclusion

It is well-documented that the poor cycling performance of $LiMn_2O_4$ (LMO) for lithium-ion batteries at elevated temperature is due to the instability of the concentration of Mn^{3+} in the spinel structure. This study describes, for the first time, the impact of microwave irradiation on LMO doped with a minute amount of nickel ($LiNi_{0.2}Mn_{1.8}O_4$, LMNO) using Mn_3O_4 prepared from electrolytic manganese oxide (EMD, γ-MnO_2) as the main precursor. From detailed spectroscopic, microscopic and electrochemical analyses, we have demonstrated that microwave irradiation could enhance the exposure of the {111} facets of the spinel and tune the Mn^{3+} concentration thereby promoting structural stability and cycling performance at elevated temperature (60 °C). Considering that the state-of-the-art methods of curbing the problem of capacity fading at elevated temperature are time-consuming and involve the use of harsh acidic treatment, the novelty of this finding gives promise for the potential adoption of a greener method of improving the electrochemical cycling performance at elevated temperatures.

Acknowledgements

This work was supported by the CSIR (South Africa), the South Africa's Department of Science and Technology (DST) and National Research Foundation (NRF). Dr Kumar Raju thanks the CSIR for post-doctoral research fellowship.

References

1 M. Yohio, *Lithium-Ion Batteries*, Springer, New York, 2008.
2 J. M. Tarascon and M. Armand, *Nature*, 2001, **414**, 359.
3 O. K. Park, Y. Cho, S. Lee, H. Yoo, H. K. Song and J. Cho, *Energy Environ. Sci.*, 2011, **4**, 1621.
4 J. B. Goodenough and Y. Kim, *Chem. Mater.*, 2010, **22**, 587.
5 M. Jo, Y. K. Lee, K. M. Kim and J. Cho, *J. Electrochem. Soc.*, 2010, **157**, A481.
6 H. Kawai, M. Nagata, H. Kageyama, H. Tukamoto and A. R. West, *Electrochim. Acta*, 1999, **45**, 315.
7 E. Hosono, T. Kudo, I. Honma, H. Matsuda and H. S. Zhou, *Nano Lett.*, 2009, **9**, 1045.
8 J. W. Fergus, *J. Power Sources*, 2010, **195**, 939.
9 B. Scrosati and J. Garche, *J. Power Sources*, 2010, **195**, 2419.
10 F. Jiao, J. L. Bao, H. A. Hill and P. G. Bruce, *Angew. Chem., Int. Ed.*, 2008, **47**, 9711.
11 M. M. Thackeray, *J. Am. Ceram. Soc.*, 1999, **82**, 3347.
12 R. J. Gummow, A. D. Kock and M. M. Thackeray, *Solid State Ionics*, 1994, **69**, 59.
13 Y. Shin and A. Manthiram, *J. Electrochem. Soc.*, 2004, **151**, A204.
14 S. Komaba, N. Kumagai and Y. Kataoka, *Electrochim. Acta*, 2002, **47**, 1229.
15 D. Aurbach, *J. Power Sources*, 2000, **89**, 206.
16 A. Blyr, C. Sigala, G. Amatucci, D. Guyomard, Y. Chabre and J.-M. Tarascon, *J. Electrochem. Soc.*, 1998, **145**, 194.
17 M. A. Andersson and K. Edström, *J. Electrochem. Soc.*, 2001, **148**, A1100.
18 A. M. Kannan and A. Manthiram, *Electrochem. Solid-State Lett.*, 2002, **5**, A167.
19 M. M. Thackeray, C. S. Johnson, J. S. Kim, K. C. Lauzze, J. T. Vaughey, N. Dietz, D. Abraham, S. A. Hackney, W. Zeltner and M. A. Anderson, *Electrochem. Commun.*, 2003, **5**, 752.
20 M. Zhang, Y. Wang, J. N. Reimers and M. Gee, European Patent (EP) 1056143B1, 2007.
21 G. Amatucci, A. Du Pasquier, A. Blyr, T. Zheng and J.-M. Tarascon, *Electrochim. Acta*, 1999, **45**, 255.
22 N. M. Hagh, F. Cosandey, S. Rangan, R. Bartynski and G. Amatucci, *J. Electrochem. Soc.*, 2010, **157**, A305.
23 S. T. Myung, K. S. Lee, D. K. Kim, B. Scrosati and Y. K. Sun, *Energy Environ. Sci.*, 2011, **4**, 935.
24 G. P. Zhong, Y. Y. Wang, X. J. Zhao, Q. S. Wang, Y. Yu and C. H. Chen, *J. Power Sources*, 2012, **216**, 368.
25 L. S. Yong and F. Li, US Patent Application, 2012/0237837 A1, 2012.

26 K. R. Chemelewski, E. S. Lee, W. Li and A. Manthiram, *Chem. Mater.*, 2013, **25**, 2890.
27 B. Hai, A. K. Shukla, H. Duncan and G. Chen, *J. Mater. Chem. A*, 2013, **1**, 759.
28 Y. J. Wei, L. Y. Yan, C. Z. Wang, X. G. Xu, F. Wu and G. Chen, *J. Phys. Chem. B*, 2004, **108**, 18547.
29 M. A. Kebede, N. Kunjuzwa, C. J. Jafta, M. K. Mathe and K. I. Ozoemena, *Electrochim. Acta*, 2014, **128**, 172.
30 C. J. Jafta, M. K. Mathe, N. Manyala, W. D. Roos and K. I. Ozoemena, *ACS Appl. Mater. Interfaces*, 2013, **5**, 7592.
31 N. P. Funeka, C. J. Jafta, M. Kebede, L. le Roux, M. K. Mathe and K. I. Ozoemena, *RSC Adv.*, 2015, **5**, 32256.
32 S. Komaba, T. Tsuchikawa and A. Ogata, *ECS Trans.*, 2008, **16**, 201.
33 K. Yang, J. Su, L. Zhang, Y. Long, X. Lv and Y. Wen, *Particuology*, 2012, **10**, 765.
34 A. Manthiram, K. R. Chemelewski and E. S. Lee, *Energy Environ. Sci.*, 2014, **7**, 1339.
35 P. Mustarelli, V. Massarotti, M. Bini and D. Capsoni, *Phys. Rev. B: Condens. Matter Mater. Phys.*, 1997, **55**, 12018.
36 Y. J. Lee, C. Eng and C. P. Grey, *J. Electrochem. Soc.*, 2001, **148**, A249.
37 Y. J. Lee, F. Wang, S. Mukerjee, J. McBreen and C. P. Grey, *J. Electrochem. Soc.*, 2000, **147**, 803.
38 Y. J. Lee, F. Wang and C. P. Grey, *J. Am. Chem. Soc.*, 1998, **120**, 12601.
39 D. Aurbach, K. Gamolsky, B. Markovsky, G. Salitra, Y. Gofer, U. Heider, R. Oesten and M. Schmidt, *J. Electrochem. Soc.*, 2000, **147**, 1322.
40 D. Lu, W. Li, X. Zuo, Z. Yuan and Q. Huang, *J. Phys. Chem. C*, 2007, **111**, 12067.
41 Q. C. Zhuang, T. Wei, L. L. Du, Y. L. Cui, L. Fang and S. G. Sun, *J. Phys. Chem. C*, 2010, **114**, 8614.
42 M. Mohamedi, M. Makino, K. Dokko, T. Itoh and I. Uchida, *Electrochim. Acta*, 2002, **48**, 79.
43 M. Hirayana, H. Ido, K. Kim, W. Cho, K. Tamura, J. Mizuki and R. Kanno, *J. Am. Chem. Soc.*, 2010, **132**, 15268.
44 C. J. Jafta, K. I. Ozoemena, M. K. Mathe and W. D. Roos, *Electrochim. Acta*, 2012, **85**, 411.
45 J. Xiao, X. Chen, P. V. Sushko, M. L. Sushko, L. Kovarik, J. Feng, Z. Deng, J. Zheng, G. L. Graff, Z. Nie, D. Choi, J. Liu, J. G. Zhang and M. S. Whittingham, *Adv. Mater.*, 2012, **24**, 2109.
46 J. Zheng, J. Xiao, X. Yu, L. Kovarik, M. Gu, F. Omenya, X. Chen, X. Q. Yang, J. Liu, G. L. Graff, M. S. Whittingham and J. G. Zhang, *Phys. Chem. Chem. Phys.*, 2012, **14**, 13515.
47 H. M. Cho and Y. S. Meng, *J. Electrochem. Soc.*, 2013, **160**, A1482.
48 M. Gasgnier, L. Albert, J. Derouet and L. Beaury, *J. Alloys Compd.*, 1993, **198**, 73.